

Cite this: DOI: 00.0000/xxxxxxxxxx

Local Structure and Lithium Ion Diffusion Pathway of Cubic $\text{Li}_7\text{La}_3\text{Zr}_2\text{O}_{12}$ Studied by Total Scattering and the Reverse Monte Carlo Method[†]

Haolai Tian,^{*a} Martin T. Dove,^{b‡} and Xiang Yang Kong^c

Received Date

Accepted Date

DOI: 00.0000/xxxxxxxxxx

The basic perovskite network AX_3 , consisting of corner-linked octahedral groups of atoms, has for a long time known to have an inherent flexibility involving rotations of the octahedra. This is often associated with both displacive phase transitions and negative thermal expansion.

1 Introduction

Lithium ion batteries have wide application on electric vehicles, mobile devices, and battery farms for renewable energy storage. However the commonly used liquid-based electrolytes have disadvantages such as flammability, volatile and operating temperature limitations. Although all-solid-state lithium ion batteries (SSLBs) which are expected to enhance the safety reliability and performance issues have been long sought, the conductivity of solid electrolytes can not keep competing at the level of the existed liquid-based counterpart. Most solid electrolytes required both high Li^+ conductivity and negligible electronic conductivity have either high ionic conductivity or high electrochemical stability, which are not suitable for commercialized battery applications. Recently the garnet-structured $\text{Li}_7\text{La}_3\text{Zr}_2\text{O}_{12}$ (LLZO)[?] has attracted much attention as a potential solid electrolyte, which possessed high Li^+ conductivity, stability against chemical reaction with Li metal, moisture, air, as well as a wide potential window. However, LLZO exhibits two phases[?] cubic and tetragonal, which represent different Li^+ conductivity. The conductivity of the cubic phase is two orders of magnitude higher than tetragonal one, $3 \times 10^{-4} \text{ S/cm}^2$ and $1.63 \times 10^{-6} \text{ S/cm}^2$, separately. This difference may be related to the distances between Li sites, disorder degree of Li atom, and isotropic diffusion pathways in the cubic phase. A cubic garnet structure can be described[?] as $\text{A}_3\text{B}_3\text{C}_2\text{O}_{12}$ array, that La occupies B sites in 8 oxygen coordinated, Zr occupies octahedral C, and Li occupies A in tetrahedral coordination. The $\text{B}_3\text{C}_2\text{O}_{12}$ structure[?] is a host framework that contains the A-sited Li (labeled Li1) and additional unoccupied Li (labeled Li2)

in distorted octahedral coordination. A Li diffusion loop is constructed by Li1 and Li2 sites, and forms the 3-D Li^+ diffusion pathway connected by shared Li1 site.

2 Experimental methods

2.1 Synthesis

The precursor materials used were anhydrous LiOH (Alfa Aesar 99.5%, dried at 200 °C overnight; 10 wt.% excess was taken to compensate for the loss of lithium under annealing conditions), La_2O_3 (Alfa Aesar, treated at 950 °C overnight), ZrO_2 (Alfa Aesar, 99.7%). The reactants were mixed with a mortar and pestle before reacting them at 950 °C for 12 hours. The resultant product was reground and pressed into pellets. The pellets were transferred to an alumina crucible and buried with mother powder, followed by sintering at 1140 °C for 20 hours to form single-phase material. The resulting pellets were grounded into powder and stored in an Ar-filled glovebox (<0.1 ppm O_2 , <0.1 ppm H_2O) to prevent reaction with humidity.

2.2 Neutron Powder Diffraction and Total Scattering

Neutron powder diffraction and total scattering data were obtained at a number of temperatures on the GEM diffractometer at the ISIS spallation neutron source, Rutherford Appleton Laboratory, UK. The LLZO sample was contained in a cylindrical thin-walled vanadium can of 8 mm diameter. This was mounted in a standard vanadium-foil furnace for measurements at and above room temperature (at 293K, 450K, 600K, 750K, 900K and 1100K). Data were collected on six separate occasions, counting for between 5 and 6 hours per temperature. Measurements were also performed on an empty vanadium can, the empty instrument, and an 8 mm diameter vanadium rod for normalisation and background subtraction. Those data were processed by the GudrunN software to obtain scattering data $I(Q)$ and PDF data $D(r)$ with a maximum momentum transfer of Q_{max} of 50 \AA^{-1} . Diffraction data were also corrected and reduced using Mantid,

^a China Spallation Neutron Source (CSNS), Institute of High Energy Physics (IHEP), Chinese Academy of Sciences (CAS), Dongguan 523803, China

^b Centre for Condensed Matter and Materials Physics, School of Physics and Astronomy, Queen Mary University of London, Mile End Road, London, E1 4NS, United Kingdom; E-mail: martin.dove@qmul.ac.uk

^c School of Materials Sciences and Engineering, Shanghai Jiao Tong University, Huashan Road 1954, Shanghai 200030; E-mail: xykong@sjtu.edu.cn

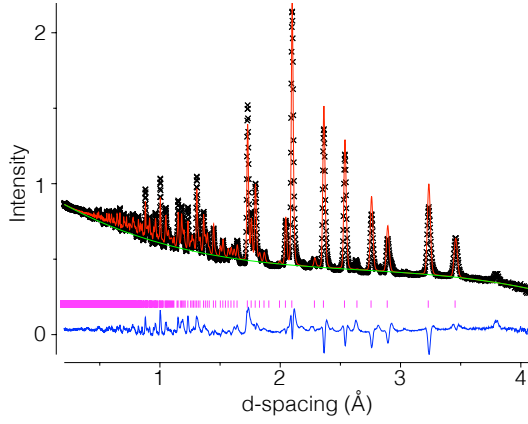


Fig. 1 Example of the quality of the Rietveld refinement of the crystal structure of LLZO from data collected from the 60° (Bank 4) at temperature of 293K.

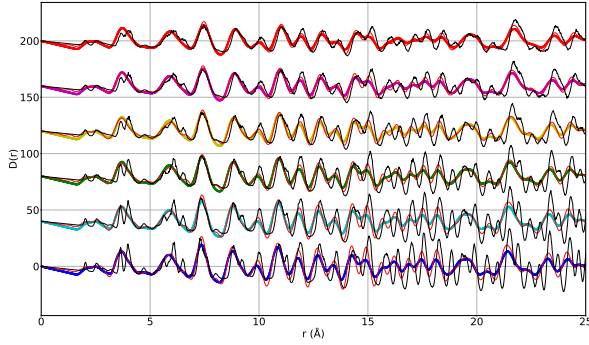


Fig. 2 Synchrotron pair distribution $D(r)$ obtained from GudrunX for all temperatures represented as circles. A constant offset has been applied to separate those curves. The solid black lines indicate the simulated intensities from DI_poly, and RMC modeling are represented by the solid red lines.

and Rietveld analysis was performed by GSAS software.

2.3 Synchrotron Total Scattering

Synchrotron powder diffraction and total scattering data were collected on the XPDF beamline (I15-1 instrument) at Diamond Light Source (UK). The X-rays were monochromatized to yield a wavelength of 0.161669 Å. The sample was sealed into borosilicate capillaries (ϕ 1 mm, and 50 mm in length) for measurements at and above room temperature (at 295K, 450K, 600K, 750K, 900K, and 1100K). The raw data were corrected and reduced into scattering data using the program DAWN⁷. And PDF $D(r)$ were processed from scattering data using GudrunX with Q-range $0.5 \leq Q \leq 25 \text{ Å}^{-1}$ for the Fourier transformation. The fluorescence corrections were applied, in which the fluorescence energy of La was assumed to be 38.739 keV.

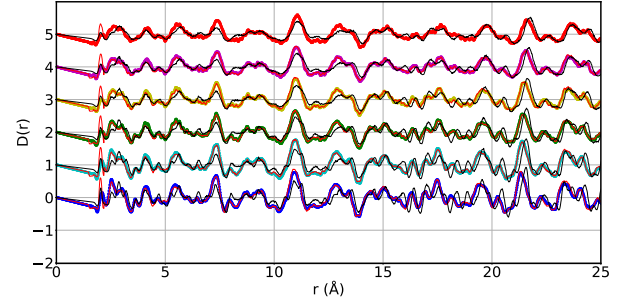


Fig. 3 Neutron pair distribution $D(r)$ obtained from GudrunN for all temperatures represented as circles. A constant offset has been applied to separate those curves. The solid black lines indicate the simulated intensities from DI_poly, and RMC modeling are represented by the solid red lines.

2.4 Pair Distribution Function (PDF)

In the diffraction theory, the differential cross section is defined as

$$\frac{1}{N} \frac{d\sigma}{d\Omega} = I(Q) = I^S(Q) + i(Q) \quad (1)$$

where $I^S(Q) = \sum_{i=1}^n c_i \frac{\sigma_i}{4\pi}$ is the self-scattering of all atoms, and $i(Q)$ is the total scattering structure factor in which we are interested. Here we define partial pair distribution function $g_{mn}(r)$ to present the number of atoms of type n within the shell between r and $r + dr$ centered on a particle of type m . And then the structure factor $i(Q)$ can be presented as

$$i(Q) = 4\pi\rho \int_0^\infty \sum_{m,n} c_m c_n b_m b_n r^2 [g_{mn}(r) - 1] \frac{\sin Qr}{Qr} dr \quad (2)$$

where c_m , b_m , and ρ denote the fraction of atoms of type m , the scattering length of species m , and the average atomic number density. Overall pair distribution function is defined as

$$D(r) = 4\pi\rho r \sum_{m,n} c_m c_n b_m b_n [g_{mn}(r) - 1] \quad (3)$$

The $D(r)$ can be calculated via Fourier transformation of $i(Q)$

$$D(r) = \frac{2}{\pi} \int_0^{Q_{max}} M(Q) Q i(Q) \sin Qr dr \quad (4)$$

where $M(Q)$ is the Lorch function to reduce the effect of finite maximum momentum transfer, Q_{max} . Those tasks were carried out using the program GudrunX and GudrunN.

2.5 Reverse Monte Carlo Analysis (RMC)

Involving measurements of the total neutron and X-ray powder diffraction, the RMC Profile program combines and fits all the reciprocal $i(Q)$, real-space $D(r)$ data, and the intensities of the Bragg peaks at the same time. The explicit use of the Bragg intensities ensures that the RMC refinement gives configurations that have the correct long-range average structure and symmetry without any exaggeration of the structural disorder. The traditional Metropolis Monte Carlo algorithm moves atoms randomly to generate new configuration. In order to keep atomic movement

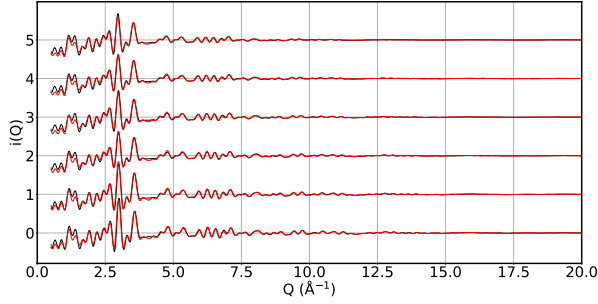


Fig. 4 Neutron scattering function $S(Q)$ for all temperatures. A constant offset has been applied to separate those curves.

within the crystal structure, maximum atomic moves of La, O and Zr were of size 0.05, but those of Li were 0.1. The minimum distances between pairs of atoms are give in Table 1.

χ^2 is definded to reflect the agreement between calculated (Monte Carlo) and observed (measured) curves

$$\chi^2 = \sum_j \sum_i (y_{i,j}^{obs} - y_{i,j}^{calc})^2 / \sigma_j \quad (5)$$

where $y_{i,j}^{obs}$ is the observed values at data point i in data set j , $y_{i,j}^{calc}$ is the calculated counterpart, and σ_j is the weighing that represents the statistical accuracy of data set. In this study, data sets include $i(Q)$ from both neutron and synchrotron power diffraction, and $D(r)$ and Bragg data from neutron diffraction only, all with equal σ_j . An atomic move can be accepted when the value of χ^2 declines. If the value of χ^2 raises by $\Delta\chi^2$, the probability of acception is $\exp(-\Delta\chi^2/2)$

The initial RMC configuration were generated from the crystal strucutres got by Rietveld refinement of neutron diffraction. Each contained $4 \times 4 \times 4$ unit cells with 12288 atoms. And the RMC analysis were run for long enough to ensure the convergence of the simulation by checing the value of χ^2 .

Table 1 The minimum distances between pairs of atoms

	Li	O	Zr	La
Li	1.69	1.50	2.3	2.3
O		2.2	1.79	2.2
Zr			5.0	3.3
La				3.3

2.6 Molecular Dynamic Simulation (MD)

Classical MD simulations were performed on $4 \times 4 \times 4$ unit cells and 12288 atoms of LLZO using the DL_POLY package. Empirical force-fields similar to previous work were employed which include the long-range Coulombic potential, short-range Buckingham potential, and Dick-Overhauser core-shell potential for O atoms. The parameters of force-field are listed in Table 2. Constant number, volume, and energy (NVE) ensemble simulations were carried out at 300K, 450K, 600K, 750K, 900K and 1100K. Each initial configurations came from the result of RMC analysis

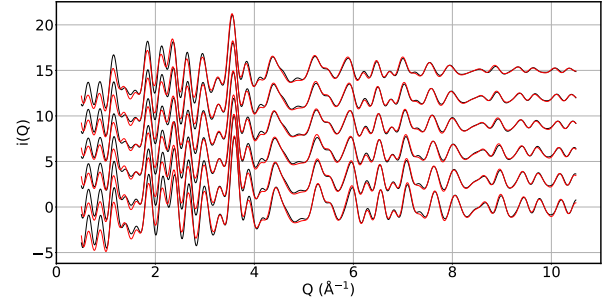


Fig. 5 Synchrotron scattering function $S(Q)$ for all temperatures. A constant offset has been applied to separate those curves.

at same temperature. The simulations were performed for 10 ps with atomic positions saved every 0.01 ps.

Table 2 Force-field parameters

	Buckingham parameters			O shell parameters	
	A (eV)	ρ (Å)	C (eVÅ ⁶)	Y (e)	k (eV ⁻²)
Zr-O	1385.02	1.79	0		-2.76
La-O	4579.23	0.3044	0		30.2
Li-O	632.102	0.2906	0	m (au)	0.2
O-O	22764.30	0.1490	27.63		

2.7 GASP analysis

Both our RMC and MD configurations have been analysed using the GASP method. In this method the motions of the atoms associated with each polyhedron in the configuration are described together as a combination of whole-polyhedron rotation, bond-bending and bond-stretching motions.

3 Results and discussion

3.1 Crystal Structure Analysis

The structural parameters of Rietveld refinement for all temperatures are listed in Table 3, which fitted well to the cubic model with space group $Ia\bar{3}d$. A sample fit to the data, namely for the data at 293K, is shown in Fig.1 The lattice parameters are plotted as functions of temperature in Fig.6, showing a linear thermal expansion.

the average structure calculated from the RMC configurations agreed well with Rietveld refinement, as shown in Fig. 7

3.2 Local Structure Analysis

The synchrotron pair distribution function $D(r)$ defined as functions 3 and 4, are shown in Fig. 2. The first peak corresponds to the La-O nearest-neighbor distance at around 2.5 Å, and the second peaks refers to La-Zr around 3.6 Å. The position and integrated area are constant for all temperatures, reflection there is no significant differences in crystal framework structure. The higher- r PDF shows shifting and broadening of the peaks as the temperature rising, because of the increases of the lattice parameters.

Table 3 Cell parameters and atomic fractional coordinates of LLZO. Zr has fractional coordinates 0,0,0, La has fractional coordinates 0.125,0,0.25, and Li1 has fractional coordinates 0.25,0,0.125.

T(K)	a(Å)	O_x	O_y	O_z	$Li2_x$	$Li2_y$	$Li2_z$
273	12.921935	0.101587	0.196351	0.282562	0.125	0.174334	0.424334
450	12.952953	0.102189	0.196519	0.281758	0.125	0.187500	0.437500
600	12.980208	0.102160	0.197170	0.281250	0.125	0.187500	0.437500
750	13.009548	0.101086	0.195999	0.282573	0.125	0.172539	0.422539
900	13.045011	0.102160	0.197170	0.281250	0.125	0.187500	0.437500
1100	13.086332	0.101519	0.197491	0.282502	0.125	0.177546	0.427546

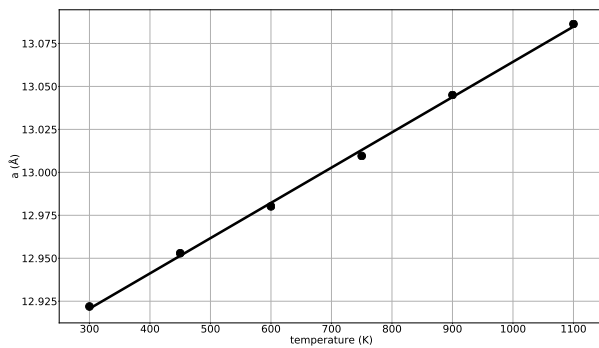


Fig. 6 Variation of the lattice parameters with temperature, obtained by Rietveld analysis.

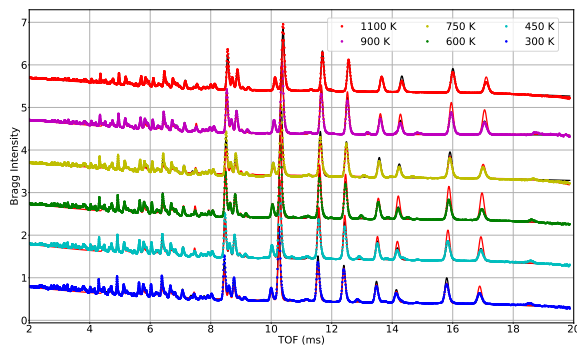


Fig. 7 The Bragg diffraction data. The data are represented as circles with constant offset to separate those curves. The solid black lines indicate the calculated intensities from GSAS, and RMC modeling are represented by the solid red lines.

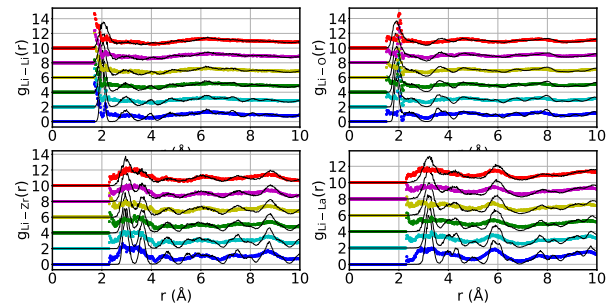


Fig. 8 The distributions calculated from RMCProfile of (1) Li-Li, (2) Li-O, (3) Li-Zr, (4) Li-La at low- r range for all temperatures. A constant offset has been applied to separate those curves.

The RMC analysis used 4 data sets to perform RMC fits, including Bragg data (Fig.7) and PDF $D(r)$ from neutron total scattering (Fig.3), and scattering function $i(Q)$ from both neutron (Fig.4) and synchrotron experiments (Fig.5).

The low- r distributions of distances from the RMC and MD configurations are shown in Fig.8 and Fig.9. The interesting point about these diagrams is that the Li-X (X represents Li, La, Zr or O) distribution from RMC are smoother than those from MD in all temperatures, as shown in Fig.8, indicating the Li-ion movement remains disorderly. But the framework structure keep stable in each case as shown in Fig.9, which is consist with the result of XPDF as shown in Fig. 2.

3.3 Lithium Distribution and Dynamics Analysis

The 3D density maps of Li in cubic garnets are shown in Fig.10. The lithium distribution can be expected in liquid and amorphous materials

4 Conclusions

The conclusions section should come in this section at the end of the article, before the Conflicts of interest statement.

5 Appendix

5.1 The Correlation Functions

Time-dependent correlation functions are valuable tools to describe the average way the quantity will change with time, and predict the trends within the behaviour of atomic structure and dynamics.

One of the simplest correlation function for velocity with a

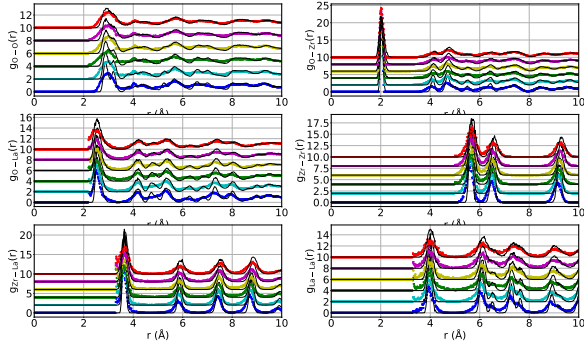


Fig. 9 The distributions calculated from RMCPProfile of (1) O-O; (2) O-Zr; (3) O-La; (4) Zr-Zr; (5) Zr-La; (6) La-La at low- r range for all temperatures. A constant offset has been applied to separate those curves. The solid lines (black) indicate the values obtained from Molecular Dynamic simulation

mean value of zero, $C(t)$, is defined as

$$C(t) = \frac{\langle v(0)v(t) \rangle}{\langle |v(0)|^2 \rangle} = \frac{(\lim_{\mathcal{T} \rightarrow \infty} \frac{1}{\mathcal{T}} \int_0^{\mathcal{T}} v(t')v(t+t')dt')}{\langle v^2 \rangle} \quad (6)$$

For the harmonic crystal, the velocity of the j -th atom is given as

$$v_j(t) = \frac{-i}{(Nm_j)^{1/2}} \sum_{\mathbf{k}, \nu} \omega(\mathbf{k}, \nu) \mathbf{e}_j(\mathbf{k}, \nu) \exp(i\mathbf{k} \cdot \mathbf{r}) Q(\mathbf{k}, \nu, t) \quad (7)$$

and leads to the classical result:

$$\sum_j m_j \langle |v_j(t) \cdot v_j(0)| \rangle = \frac{k_B T}{N} \sum_{\mathbf{k}, \nu} \cos(\omega(\mathbf{k}, \nu)t) \quad (8)$$

In addition, the power spectra $Z(\omega)$ is given by the Fourier transform of $C(t)$:

$$Z(\omega) = \int C(t) \exp(-i\omega t) dt \quad (9)$$

It can be seen that the power spectrum of the mass-weighted velocity correlation function is equal to the phonon density of states.

Consider another correlation function for position of atom, $G_s(r, t)$, is defined as

$$\begin{aligned} G_s(\Delta r, t) &= \frac{\langle r(0)r(t) \rangle}{\langle |r(0)|^2 \rangle} \\ &= \frac{1}{N} \sum_j \int \langle \delta(r' - r_j(0)) \delta(r' + \Delta r - r_j(t)) dr' \rangle \\ &= \frac{1}{N} \langle \sum_j \delta(\Delta r + r_j(0) - r_j(t)) \rangle \end{aligned}$$

which is related to the probability of finding an atom in the volume dr at position Δr for a time interval of t , and can be named as self-part of van Hove correlation function.

The mean square displacement (MSD) $\langle \Delta r_i(t) \rangle^2$ is a measure of the deviation of the position of an atom with respect to a reference position over time. MSD is related to the $G_s(r, t)$ as:

$$\langle \Delta r_i(t) \rangle^2 = \int_0^\infty (\Delta r_i(t))^2 \cdot 4\pi (\Delta r_i(t))^2 G_s(\Delta r, t) d\Delta r \quad (10)$$

Conflicts of interest

There are no conflicts to declare.

Acknowledgements

The Acknowledgements come at the end of an article after Conflicts of interest and before the Notes and references.

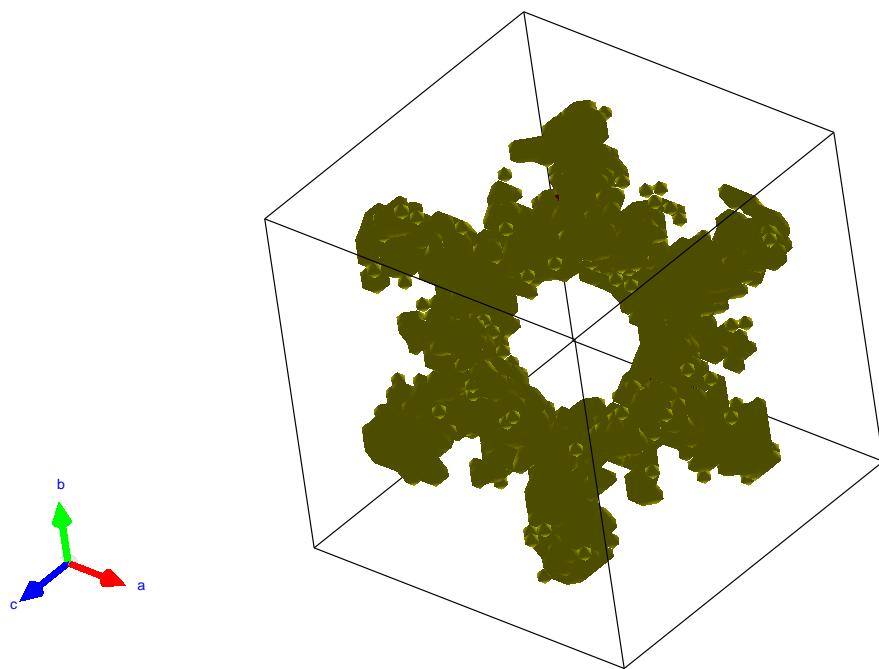


Fig. 10 Isosurfaces with level of 0.1 \AA^{-3} (yellow) and 3 \AA^{-3} (red)

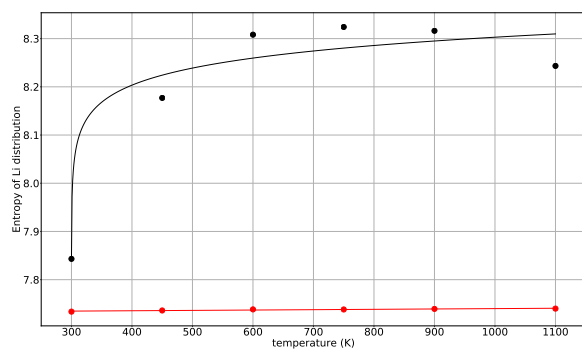


Fig. 12 The entropy of Li distribution. Data represented by black circles are the experimentally determined values using RMC refinement. Red circles represent the Molecular Dynamic simulation ones.

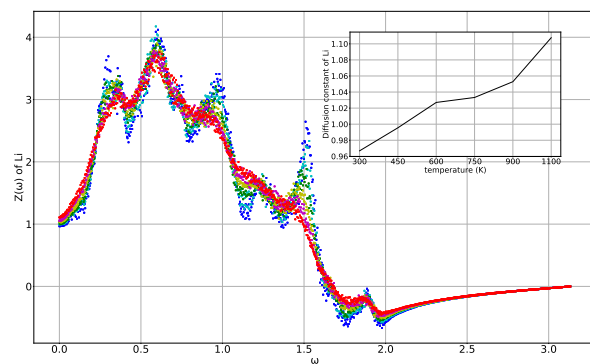


Fig. 13 The power spectrum of Li vibrational frequencies. The zero point of power spectrum for each temperature yields the diffusion constant. The inset shows a diffusion constant (D) versus temperatures.

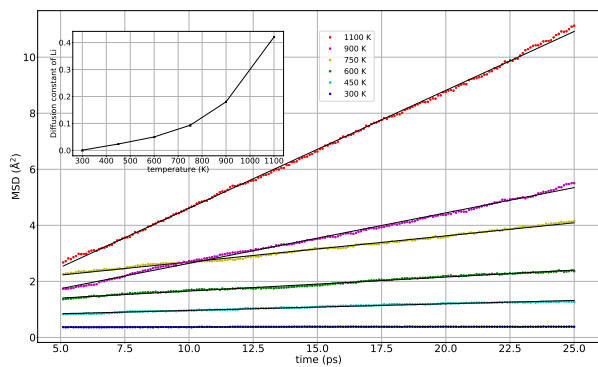


Fig. 11 Mean squared displacement (MSD) of Li from 300 K to 1100 K. The slope of MSD of each temperature data set yields the diffusion constant (D). The inset shows a diffusion constant (D) versus temperatures.